PNAS RESEARCH ARTICLE | ECOLOGY
ENVIRONMENTAL SCIENCES

El Niño-Southern Oscillation forcing on carbon and water cycling in a Bornean tropical rainforest

Naoya Takamura[a,1], Yoshiaki Hata[a,1], Kazuho Matsumoto[b], Tomonori Kume[c], Masahito Ueyama[d], and Tomo'omi Kumagai[a,e,f,2]

Edited by Steven Wofsy, Harvard University, Cambridge, MA; received January 29, 2023; accepted August 15, 2023

Carbon dioxide and water vapor exchanges between tropical forest canopies and the atmosphere through photosynthesis, respiration, and evapotranspiration (ET) influence carbon and water cycling at the regional and global scales. Their inter- and intra-annual variations are sensitive to seasonal rhythms and longer-timescale tropical climatic events. In the present study, we assessed the El Niño-Southern Oscillation (ENSO) influence on ET and on the net ecosystem exchange (NEE), using eddy-covariance flux observations in a Bornean rainforest over a 10-y period (2010–2019) that included several El Niño and La Niña events. From flux model inversions, we inferred ecophysiological properties, notably the canopy stomatal conductance and "big-leaf" maximum carboxylation rate (V_{cmax25_BL}). Mean ET values were similar between ENSO phases (El Niño, La Niña, and neutral conditions). Conversely, the mean net ecosystem productivity was highest during La Niña events and lowest during El Niño events. Combining Shapley additive explanation calculations for nine controlling factors with a machine-learning algorithm, we determined that the primary factors for ET and NEE in the La Niña and neutral phases were incoming shortwave solar radiation and V_{cmax25_BL}, respectively, but that canopy stomatal conductance was the most significant factor for both ET and NEE in the El Niño phase. A combined stomatal-photosynthesis model approach further indicated that V_{cmax25_BL} differences between ENSO phases were the most significant controlling factor for canopy photosynthesis, emphasizing the strong need to account for ENSO-induced ecophysiological factor variations in model projections of the long-term carbon balance in Southeast Asian tropical rainforests.

Southeast Asian tropics | eddy covariance | photosynthesis | transpiration | two-big-leaf model

Significance

Tropical rainforest–atmosphere exchanges of carbon dioxide and water vapor are essential for the carbon balance and represent a major source of global hydrological fluxes. Their interannual variations in a Bornean rainforest are likely induced by the El Niño-Southern Oscillation (ENSO) and regulate the global carbon and water cycles, but the controlling processes remain poorly understood. Combining 10 y of field observations that included several ENSO events with a canopy photosynthesis model to derive key ecophysiological traits, such as photosynthetic capacity and stomatal conductance, we investigated the influence of meteorological and biological drivers on forest–atmosphere exchanges in each ENSO phase. We established that ENSO-induced ecophysiological factor variations primarily influenced the long-term carbon cycle in Southeast Asian tropical rainforests.

Tropical forests play an essential role in the global carbon cycle (1, 2) and generate major hydrological fluxes that influence the climate and the water cycle at the regional and global scales (3, 4). Exchanges of carbon dioxide (CO_2) and water vapor (H_2O) between the forest canopy and the atmosphere through photosynthesis, respiration, and evapotranspiration (ET) contribute strongly to carbon and water cycling in a forest ecosystem. Inter- and intra-annual variations of meteorological drivers and ecophysiological traits control such exchanges, thereby regulating the forest ecosystem productivity and water use. Bornean tropical rainforests in the Southeast Asian tropics are among the moistest world biomes, with abundant rainfall and high temperatures throughout the year (5), and intense CO_2 and H_2O exchanges that exhibit limited seasonality in such climatic conditions. However, the warm (El Niño) and cold (La Niña) phases of the El Niño-Southern Oscillation (ENSO) induce droughts and periods of increased humidity, respectively, causing interannual meteorological variations in the western Pacific (6, 7). Furthermore, climate models project an increase in the frequency and intensity of future El Niño and La Niña events in response to global warming (8). This will likely induce severe droughts and devastating floods in the Southeast Asian tropics (8). Because tropical rainforests are crucial for climate mitigation through carbon sequestration and ET (9, 10), the relationship between ENSO-induced climatic conditions and CO_2 and H_2O canopy exchanges in Southeast Asian rainforests must be characterized. The limited availability of long-term, large-scale field measurements explains the considerable remaining uncertainty in current assessments of the carbon and water cycles in Southeast Asia. The analysis of such measurements is the purpose of this study.

Previous studies established a connection between severe El Niño-induced droughts and reduced terrestrial carbon uptake, using observations from multiple satellites (11) or combining satellite-based remote-sensing data and diagnostic modeling (12, 13). Additional studies characterized the relationship between El Niño events and the carbon balance by combining model simulations, remote-sensing data, and ground-based observations such as eddy flux tower data (14, 15). Moreover, detailed investigations of leaf-to-individual-level physiology demonstrated stomatal closure under severe El Niño-induced drought conditions (16, 17), resulting in carbon uptake reduction (17).

Author contributions: T. Kumagai designed research; N.T., Y.H., K.M., T. Kume, M.U., and T. Kumagai performed research; N.T. and Y.H. analyzed data; N.T. implemented the model and provided comments; Y.H. processed micrometeorological data and provided comments; K.M. and T. Kume collected data, maintained the micrometeorology instruments, and provided comments; M.U. implemented the model and provided comments; and T. Kumagai wrote the paper.

The authors declare no competing interest.

This article is a PNAS Direct Submission.

[1]N.T. and Y.H. contributed equally to this work.

[2]To whom correspondence may be addressed. Email: tomoomikumagai@gmail.com.

This article contains supporting information online at https://www.pnas.org/lookup/suppl/doi:10.1073/pnas.2301596120/-/DCSupplemental.

Published October 9, 2023.

To improve terrestrial ecosystem model projections of the carbon and water cycle response to climate-change-induced extreme conditions in Southeast Asian tropical forests, continuous long-term field tower measurements of eddy flux and micrometeorological variables are necessary. Using such measurements, the mechanistic relationships between meteorological drivers, ecophysiological traits, and the resulting canopy exchanges can be characterized during both El Niño and La Niña events.

Here, we report on an eddy-covariance flux observation campaign (*SI Appendix*, Fig. S1) in a natural tropical rainforest of the Lambir Hills National Park, Sarawak, Malaysia (5). The campaign lasted approximately 10 y (late 2009–2019) and included several El Niño and La Niña events, defined from monthly values of the multivariate ENSO index (MEI.v2, retrieved from https://psl.noaa.gov/enso/mei/; *SI Appendix*, Fig. S2). Eddy-covariance measurements were acquired using a 90-m-tall canopy crane over a forest canopy with an approximate height of 40 m. Continuous data for ET and the net ecosystem CO_2 exchange (NEE) were derived from the eddy-covariance data. In this study, we first assess the influence of ENSO events on meteorological drivers (e.g., precipitation or incoming shortwave solar radiation), ecosystem fluxes (e.g., ET), net ecosystem productivity (NEP, with NEP = −NEE), and ecophysiological traits (e.g., canopy stomatal conductance or "big-leaf" maximum carboxylation rate) calculated with an inverse eddy-covariance flux model [(18); see *Materials and Methods* and *SI Appendix*). Then, we infer the dependence of ET and NEE on meteorological drivers and ecophysiological traits under El Niño, La Niña, and neutral conditions by using Shapley additive explanation [SHAP; (19); *Materials and Methods*] values, calculated for nine controlling factors, as input for a machine-learning prediction algorithm ["gradient-boosted regression trees"; (20)]. Such analyses, rarely available for tropical forests, are enabled by the duration, continuity, and high temporal resolution of the collected field data. Finally, on the basis of the SHAP analysis results, we apply a combined stomatal-photosynthesis model approach (21) to the field data, which allows us to establish that ENSO-induced changes in ecophysiological traits exerted the strongest influence on long-term ecosystem flux variations. Therefore, our study demonstrates that understanding the ENSO control mechanisms of ET and NEE is essential to refine terrestrial model projections of carbon and water cycling in Southeast Asian tropical rainforests.

Comparison of ET, NEE, and NEP in the El Niño, La Niña, and Neutral Phases

We classified ecosystem fluxes, meteorological drivers, and ecophysiological traits into subsets representative of El Niño, La Niña, or neutral ENSO conditions as defined with the MEI.v2 (*SI Appendix*, Fig. S2). Monthly mean values calculated for meteorological variables over the study period (*SI Appendix*, Fig. S3) were lower for precipitation (P) and higher for incoming shortwave solar radiation (R_s), air temperature (T_a), and atmospheric humidity deficit (D) during El Niño events than under neutral conditions. Conversely, monthly means were higher for P and lower for R_s, T_a, and D during La Niña events than under neutral conditions. We also analyzed mean diurnal variations for NEE and ET over the study period (*SI Appendix*, Fig. S4). Midday means (10:00–14:00 local time) in the El Niño, neutral, and La Niña phases were −20.3 μmol m^{-2} s^{-1}, −23.8 μmol m^{-2} s^{-1}, and −23.8 μmol m^{-2} s^{-1}, respectively, for NEE, and 7.60 mmol m^{-2} s^{-1}, 7.90 mmol m^{-2} s^{-1}, and 7.96 mmol m^{-2} s^{-1}, respectively, for ET. Differences in meteorological conditions between the ENSO phases likely caused the differences in NEE and ET. An R_s increase, resulting from an increased occurrence of clear-sky conditions in the El Niño phase, would enhance NEE and ET. Conversely, drought conditions during El Niño events, i.e., a soil moisture content (Θ) decrease caused by decreasing P and increasing D, would induce a decrease in canopy stomatal conductance (G_c) and other ecophysiological functions, subsequently reducing ET and NEE (*SI Appendix*, Fig. S3). Such effects, opposite but with comparable magnitude, would decrease in the order La Niña ≥ neutral > El Niño (*SI Appendix*, Fig. S4), in contradiction with previous results in Amazonian tropical rainforests (22) where the photosynthetic flux, not limited by water availability but driven by incident radiative energy, exhibited higher values in the dry season than in the wet season (22).

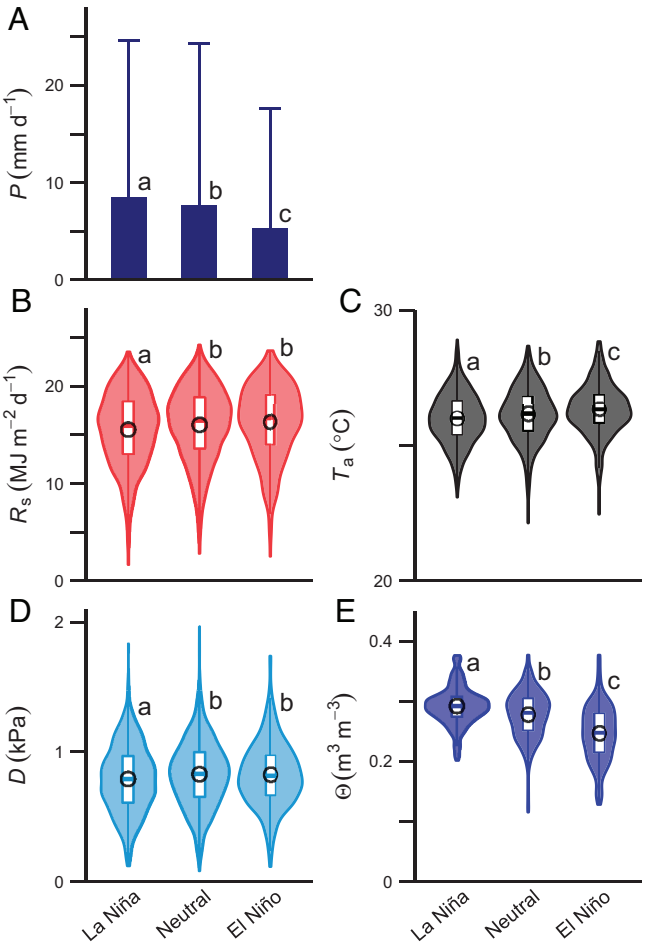

Fig. 1. Comparison of meteorological variables under La Niña (*Left*), neutral (*Center*), and El Niño (*Right*) conditions. Mean values (bars) and SD (thin vertical lines) are shown in Panel (*A*) for precipitation (*P*). Violin plots are shown for (*B*) incoming shortwave solar radiation (R_s), (*C*) air temperature (T_a), (*D*) atmospheric humidity deficit (*D*), and (*E*) volumetric soil moisture content in the 0–50 cm soil layer (Θ). The shaded area indicates the population distribution. The box-and-whisker plot within the shaded area represents the interquartile range (white box), the median value (horizontal bar within the white box), and the rest of the distribution after outlier removal (whisker). The mean value (open circle) is also indicated. Letters (a, b, or c) near each vertical line indicate significant population distribution differences between the ENSO phases (Steel–Dwass test; $P < 0.05$).

Subsequently, we investigated interannual variations of meteorological drivers (Fig. 1) and ecophysiological traits under distinct ENSO conditions and their influence on ET, NEP, and NEP components (Fig. 2). As a reference, we calculated annual values of ET, NEP, gross primary productivity (GPP), and ecosystem respiration (R_{eco}) over the study period (2010–2019; *SI Appendix*, Fig. S5). Mean annual values and associated SD were 1,412 ± 86

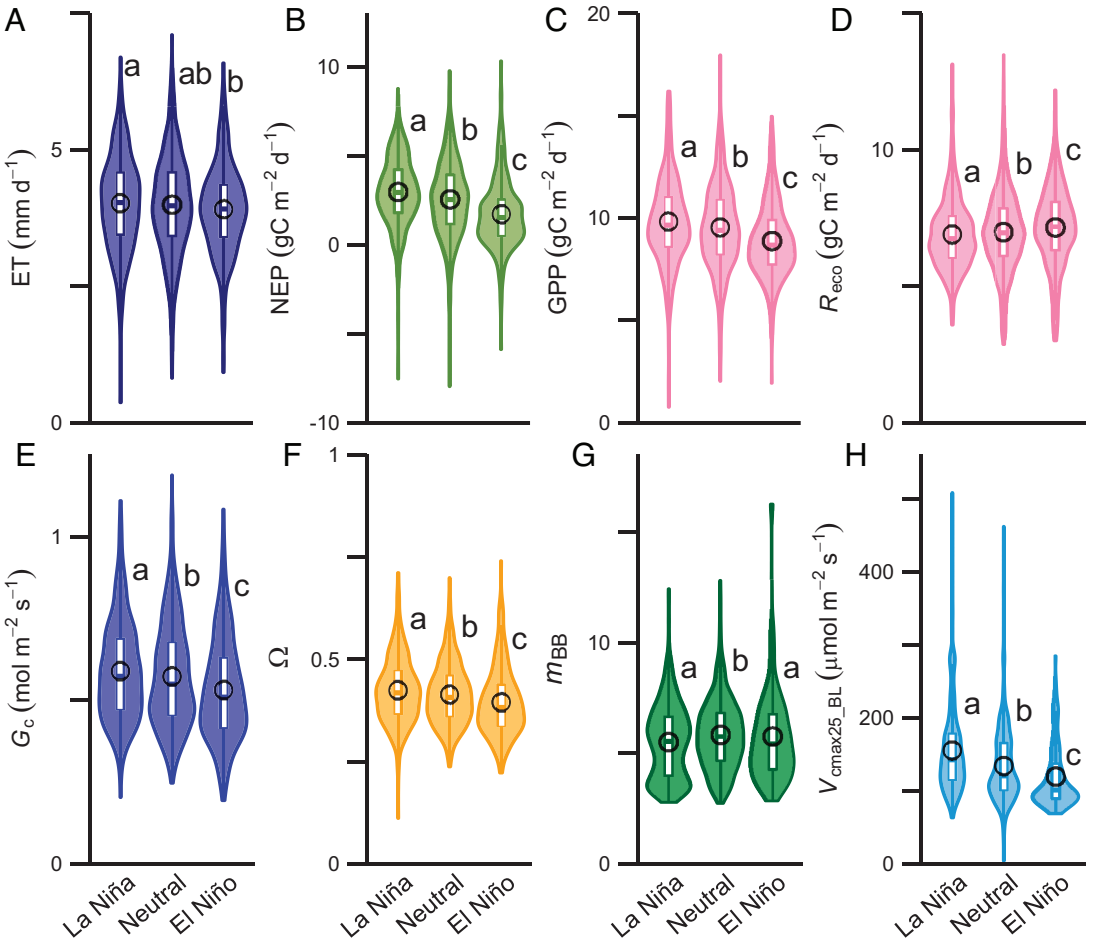

Fig. 2. Comparison of eddy-covariance fluxes and ecophysiological traits under La Niña (*Left*), neutral (*Center*), and El Niño (*Right*) conditions. Violin plots are shown for (*A*) evapotranspiration (ET), (*B*) net ecosystem productivity (NEP), (*C*) gross primary productivity (GPP), (*D*) ecosystem respiration (R_{eco}), (*E*) canopy stomatal conductance (G_c), (*F*) decoupling factor (Ω), (*G*) Ball–Berry model slope (m_{BB}), and (*H*) big-leaf maximum carboxylation rate at 25 °C (V_{cmax25_BL}). Graphical representation is the same as in Fig. 1. Letters (a, b, or c) near the top of each violin plot indicate significant population distribution differences between the ENSO phases (Steel–Dwass test; $P < 0.05$).

mm y^{-1} for ET, 8.6 ± 1.6 tC ha^{-1} y^{-1} for NEP, 34.0 ± 2.7 tC ha^{-1} y^{-1} for GPP, and 25.6 ± 1.8 tC ha^{-1} y^{-1} for R_{eco}. These were comparable to, or higher than, values reported in Amazonian tropical rainforests (22, 23), possibly because of the presence of markedly larger trees at our study site. In particular, the Bornean tropical rainforest functioned as a large carbon sink (consistently positive NEP) over the study period, with nearly constant annual mean ET, whereas Amazonian tropical rainforests were net small carbon sink with negligible or negative NEP, but also with constant annual-mean ET values in 2002–2005 (23). Although there was no clear correspondence between annual-mean values and ENSO phases because the duration of ENSO events varied markedly during the study period (from a few days to nearly 2 y), NEP decreased notably at shorter timescales, occasionally becoming negative during El Niño events (e.g., in 2015, 2016, and 2019; *SI Appendix*, Fig. S5).

Mean P and Θ values (Fig. 1 *A* and *E*, respectively) were highest during La Niña events, intermediate under neutral conditions, and lowest during El Niño events. These differences did not induce significant variations of the population distribution of the Ball–Berry stomatal conductance model slope [m_{BB}; (24); Steel–Dwass test; $P < 0.005$ and $P = 0.367$, respectively; Fig. 2*G*]. Similarly, gross canopy photosynthesis, representing GPP, also exhibited decreasing values in the order La Niña > neutral > El Niño (Steel–Dwass test; $P < 0.01$; Fig. 2*C*). Moreover, a slight decrease in atmospheric humidity (*SI Appendix*, Relative Humidity (h_s) in Eq. S8) in the neutral and El Niño phases, negatively correlated with D (Fig. 1*D*), was associated with decreasing G_c (Steel–Dwass test; $P < 0.05$; Fig. 2*E*), possibly because of the stomatal regulation required to balance carbon gain and water consumption (25). In the general case, a GPP decrease can either result from, or cause, a G_c reduction. In this study, results indicate that the GPP decrease associated with a lower big-leaf maximum carboxylation rate at 25 °C [V_{cmax25_BL}; (26); Fig. 2 *C* and *H*] primarily caused a decrease in G_c (Fig. 2*E*), which illustrated the close coupling between canopy stomatal behavior and atmospheric conditions in the El Niño phase [(27); Fig. 2*F*]. Furthermore, in the El Niño phase, the slight increase in atmospheric evaporation demand, represented by D (Fig. 1*D*), did not increase ET but on the contrary, a slight ET decrease was observed (Steel–Dwass test; $P < 0.05$; Fig. 2*A*). Finally, the small ET variations between ENSO phases (Fig. 2*A*) might be attributed to a decoupling between the canopy and the atmosphere [(27); Fig. 2*F*], inducing an increased dependence of ET on R_s, and corresponding slight decrease in R_s (Fig. 1*B*) during La Niña events.

The marked NEP decrease in the order of La Niña > neutral > El Niño (Steel–Dwass test; $P < 0.00001$; Fig. 2*B*) was caused by the combined effect of decreasing GPP (Fig. 2*C*) and increasing R_{eco} (Steel–Dwass test; $P < 0.05$; Fig. 2*D*) in the El Niño phase. As mentioned previously, the GPP decrease between ENSO phases

was associated with decreasing V_{cmax25_BL} values, in the order La Niña > neutral > El Niño (Steel–Dwass test; $P < 0.0001$; Fig. 2*H*). Lower G_c values, explained by stomatal closure under El Niño-induced drought stress, limit CO_2 diffusion to the substomatal cavity and its subsequent assimilation (28). Concurrently, stomatal closure reduces intercellular CO_2 concentration and limits leaf evaporative cooling, thus damaging the leaf photosynthetic infrastructure and causing V_{cmax25_BL} to decrease (28). Although we could not demonstrate a significant effect of soil moisture depletion (Θ decrease) on soil CO_2 efflux in a previous study at the same site (29), there remains a possibility for soil CO_2 efflux to increase with increasing temperature during El Niño events (Fig. 1*C*). Additionally, leaf respiration, a potentially significant contributor to R_{eco}, might increase in response to drier conditions (30, 31). Therefore, we postulate that El Niño-induced drought caused the noted R_{eco} increase.

Major Controlling Factors for ET and NEE Projections in the El Niño, La Niña, and Neutral Phases

In this section, we first evaluate the contribution of meteorological drivers and ecophysiological traits to ET and NEE variations by calculating the mean SHAP value for each controlling factor. Mean SHAP values for ET (Fig. 3*A*) were nearly negligible for most parameters except for R_s, G_c, and D. By order of decreasing importance, the main prediction factors for ET in the neutral and La Niña phases were R_s, G_c, and D, possibly because sufficient

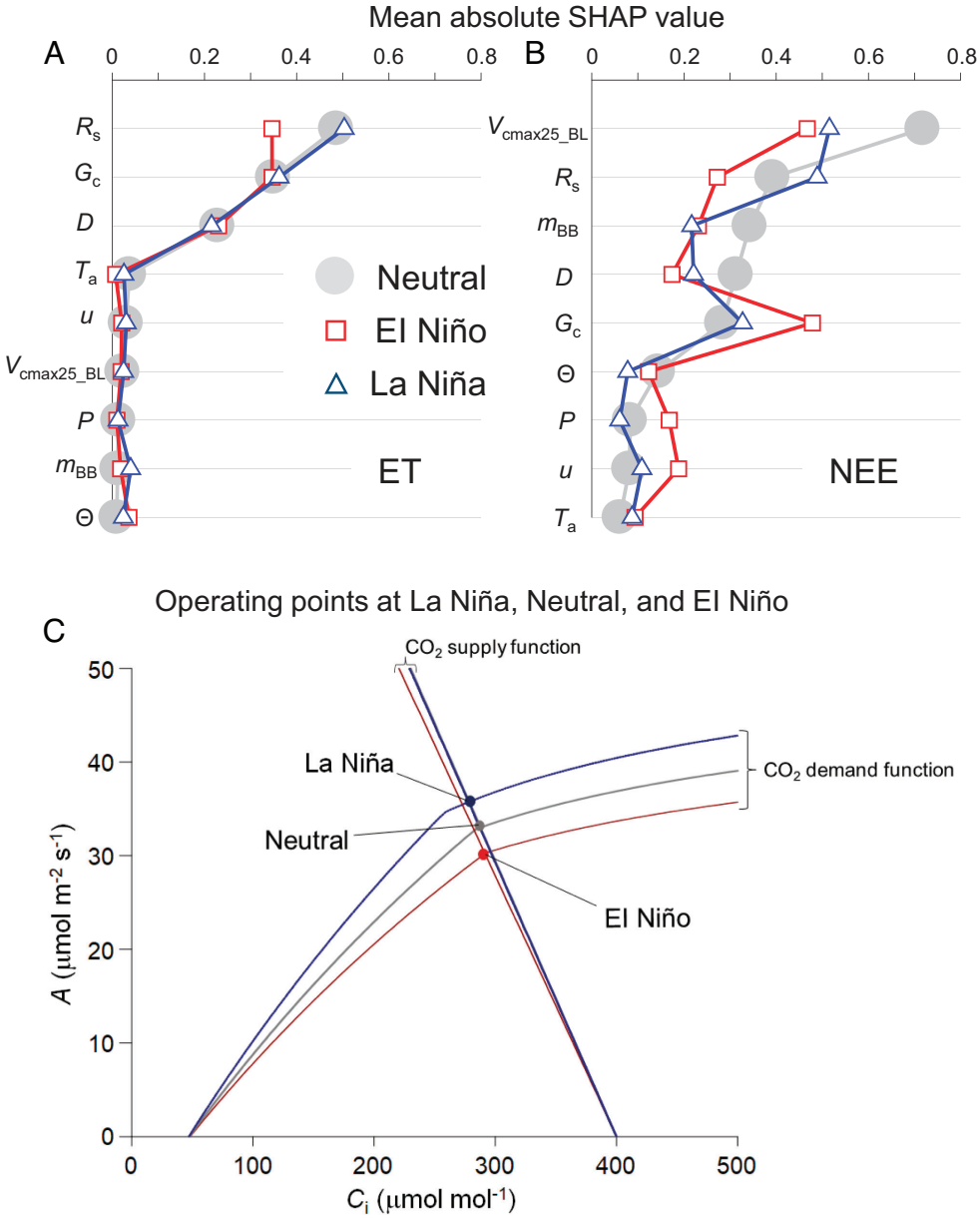

Fig. 3. Contribution of meteorological drivers and ecophysiological traits to the eddy-covariance fluxes under La Niña (blue curves and symbols), neutral (gray), and El Niño (red) conditions. Panels (*A*) and (*B*) indicate the mean Shapley additive explanation (SHAP) values over the observation period for ET and NEE, respectively. Input parameters for the tree-based machine-learning model were R_s, G_c, D, T_a, wind speed (u), V_{cmax25_BL}, P, m_{BB}, and Θ. Panel (*C*) represents the hypothetical A–C_i operating points (filled circles) for the model, determined at the intersections of the CO_2 supply and demand functions in each ENSO phase. (A) is the big-leaf photosynthesis rate and C_i is the CO_2 concentration within the big-leaf stomatal cavity. Input parameters for the supply and demand functions are given in Table 1.

stomatal opening initiated the equilibrium evaporation process that occurs theoretically at the leaf surface in water-saturated ambient air or under higher decoupling conditions [(5); Fig. 2 *E* and *F*]. Increasing G_c could not enhance ET much during equilibrium evaporation, although decreasing R_s caused an ET decrease. Conversely, the mean SHAP values in the El Niño phase were comparable for R_s and G_c, demonstrating the effect of drought on stomatal closure (Fig. 2 *E* and *F*). Consequently, the impact of the decreasing G_c and increasing R_s and D canceled out one another during El Niño events, yielding similar ET values in all ENSO phases (Figs. 1 *B* and *D* and 2 *A*, *E*, and *F* and *SI Appendix*, Fig. S4).

For NEE, mean SHAP values indicated notable differences between ENSO phases (Fig. 3*B*). Specifically, the mean SHAP value for V_{cmax25_BL} in the neutral phase was considerably higher than for other factors. By order of decreasing importance, the following factors were R_s, m_{bb}, D, and G_c (Fig. 3*B*). In the La Niña phase, the most important factors, in order of decreasing mean SHAP values, were V_{cmax25_BL}, R_s with similar values, and G_c. The mean G_c value was higher in the La Niña phase than in the neutral or El Niño phases (Fig. 2*E*). This could indicate its importance for NEE model projections. The moister La Niña environment also likely contributed to the high mean SHAP values calculated for G_c and V_{cmax25_BL}. In the El Niño phase, the mean G_c SHAP value was highest (Fig. 3*B*), implying that El Niño-induced drought had a considerable impact on stomatal closure, thus on NEP reduction (Fig. 2 *B* and *E*). Because mean SHAP values for V_{cmax25_BL} were consistently among highest in all ENSO phases, we postulate that realistic evaluation of interannual V_{cmax25_BL} variations is essential for terrestrial ecosystem models to produce accurate projections of interannual NEE variations. We describe our mechanistic analysis of NEE variations hereafter.

The big-leaf photosynthesis rate (A; μmol m^{-2} s^{-1}), equal to the GPP, can be expressed as:

$$A = \frac{G_b G_c}{1.6\left(G_b + G_c\right)}\left(C_a - C_i\right), \quad [1]$$

where G_b is the aerodynamic conductance of sensible heat (*SI Appendix*), 1.6 is the ratio of CO_2 to H_2O diffusivity in air, and C_a and C_i are the CO_2 concentrations in air (C_a = 400 μmol mol^{-1}) and within the big-leaf stomatal cavity, respectively. Additionally, A is given by the Farquhar biochemical model [(26); *SI Appendix*] as

$$A = min\left(A_v, A_j\right) - R_{d\_BL}. \quad [2]$$

The term "min(A_v, A_j)" in Eq. 2 represents the minimum of A_v and A_j. A_v and A_j are the gross photosynthesis rates limited, respectively, by ribulose 1,5-bisphosphate (RuBP) carboxylase-oxygenase activity and by the rate of RuBP regeneration through electron transport. R_{d_BL} is the big-leaf daytime respiration rate excluding photorespiration. Eqs. 1 and 2 characterize the supply of CO_2 by diffusion from the air into the big-leaf stomatal cavity (CO_2 supply function) and the net photosynthetic demand for CO_2 within the big-leaf stomatal cavity (CO_2 demand function), respectively (21).

For specific values (Table 1) of G_b, G_c, V_{cmax25_BL}, maximum big-leaf potential rate of whole-chain electron transport at 25 °C (J_{max25_BL}), big-leaf temperature (T_c), and photosynthetically active radiation (Q), the big-leaf model is characterized by specific A and C_i values determined at the intersection of the CO_2 supply and demand functions (21). Despite a slightly gentler CO_2 supply function slope in the El Niño phase explained by the low G_c, there were no significant differences in the CO_2 supply functions between the ENSO phases. The CO_2 demand functions were characterized by consistently higher A values in the order La Niña > neutral > El Niño (Fig. 3*C*). This order resulted from the competing effects of, on the one hand, T_c and Q, increasing in the order El Niño > neutral > La Niña and causing a shift of the CO_2 demand function toward higher A values, and, on the other hand, of V_{cmax25_BL} and J_{max25_BL}, increasing in the inverse order (La Niña > neutral > El Niño) and causing a stronger shift toward lower A values. A clear global relationship between V_{cmax25_BL} and J_{max25_BL} has been reported previously (32). As stated in the previous section, GPP (equal to A) was the primary controlling factor for G_c. Thus, we conclude that a detailed evaluation of V_{cmax25_BL} is critical to understand carbon and water cycling in the studied tropical rainforest ecosystem.

Table 1. Input meteorological drivers and ecophysiological traits for the CO_2 supply (Eq. 1) and demand (Eq. 2) functions plotted in Fig. 3*C*

	Units	La Niña*	Neutral*	El Niño*
G_b	mol m^{-2} s^{-1}	2.30	2.65	2.78
G_c	mol m^{-2} s^{-1}	0.588	0.572	0.531
V_{cmax25_BL}	μmol m^{-2} s^{-1}	155.4	134.2	119.8
J_{max25_BL}	μmol m^{-2} s^{-1}	308.5	257.9	222.7
T_c	°C	26.4	26.6	26.8
Q	μmol m^{-2} s^{-1}	863.3	890.4	906.4

*Input represents the mean value over the La Niña, neutral, and El Niño phases.

Finally, we discuss why, interestingly, G_c and V_{cmax25_BL} maximized in the La Niña phase, which does not represent ordinary climatic conditions (Fig. 2 *E* and *H*). From separate biometric and hydrological observations, we estimated that the 10% largest tree individuals accounted for approximately 73% and 55% of the total biomass and water use, respectively, at the studied forest stand. The stomatal opening behavior of large trees is mainly patchy, which limits leaf stomatal aperture and restricts leaf transpiration in strong sunlight, even under intermediate soil moisture conditions (33). Thus, we postulate that, during La Niña events, the observed G_c increase was caused by enhanced stomatal opening when ecosystem water resources were abundant, while the observed V_{cmax25_BL} increase was likely induced by an increased nutrient investment in the leaf photosynthetic infrastructure conditioned by the concurrent G_c increase.

Conclusions

In the western Pacific, an extreme El Niño event induces severe drought. It is frequently followed by an extreme La Niña event inducing heavy rainfall. Climate model projections indicate that the occurrence frequency of El Niño and La Niña events will increase under global warming conditions (6, 7). In this study, we characterized the response of ET and NEE to ENSO events and their interannual variations in a Southeast Asian tropical rainforest by analyzing 10 y of eddy-covariance flux observation data.

Previous studies established that, at intraannual timescales, ET in Amazonian tropical rainforests was not limited by water availability even in the dry season (22, 23). However, an intense drought that occurred in Amazonia in 2005 induced a strong decrease in forest biomass carbon associated with a notable increase

in tree mortality, even with very small GPP variations (34), possibly from hydraulic failure with excessive xylem cavitation (35). These results indicated that Amazonian tropical rainforests are less sensitive to moderately dry periods, but susceptible to hydraulic failure caused by persistent ET during severe droughts. At our study site in a Bornean tropical rainforest, similar ET values were measured throughout the study period, despite notable precipitation differences between the La Niña (more precipitation), El Niño (less precipitation), and neutral phases. However, an increase in tree mortality, observed during a past El Niño-induced severe drought in Borneo, was attributed to hydraulic failure (36). The ecosystem drought behavior at our study site, characterized by consistently high ET like in Amazonian tropical rainforests, regardless of the El Niño phase, could exacerbate the water deficit during prolonged drought periods.

In the absence of water limitations, Amazonian tropical rainforests exhibit the highest GPP in the dry season, when long periods of strong sunlight enhance the canopy photosynthetic capacity (22). Similarly, at our study site, interannual variation in canopy photosynthetic capacity, illustrated by V_{cmax25_BL} variations and controlled by water availability in each ENSO phase, was an important factor in determining GPP. Moreover, at the leaf scale, drought stress reduces the net assimilation rate by reducing stomatal conductance or the maximum carboxylation rate (28). The resulting decrease in G_c or V_{cmax25_BL} would induce a GPP reduction during droughts. Stomatal conductance generally reverts to its normal value after the drought period (28). Conversely, a decrease in the maximum carboxylation rate indicates an alteration of leaf biochemistry, longer-lasting and resource-intensive to repair (28). Therefore, characterizing the relationship between El Niño-induced drought severity and GPP reduction processes, by analyzing V_{cmax25_BL} variations, is essential to optimize dedicated submodels within terrestrial ecosystem models, thus to produce realistic projections of the long-term carbon balance in Southeast Asian tropical rainforests.

Furthermore, this study indicated higher mean NEP values under La Niña-induced moist conditions, frequently occurring after El Niño events. We believe that higher productivity in the La Niña phase compensated for the lower El Niño productivity. La Niña or El Niño events, whose duration varies from a few days to 2 y, occur every 2 to 7 y in the tropical Pacific Ocean. Thus, without decadal-scale observations, several long ENSO events that significantly influence the carbon cycle, water cycle, and ecosystem regulation mechanisms in Southeast Asian tropical rainforests would be excluded from analyses similar to those presented in this study.

Materials and Methods

Site Description. The experiment was conducted in a natural forest (4°12′N, 114°02′E, 200 masl) within the Lambir Hills National Park, 30 km south of Miri City in Sarawak, Malaysia, on the island of Borneo. The Lambir rainforest consists of two types of vegetation native to Borneo: mixed dipterocarp forest, containing various genera of the Dipterocarpaceae family and covering 85% of the Lambir Hills National Park, and tropical heath forest. The mean canopy height at the study site is approximately 40 m, but emergent treetop height can reach 50 m. The leaf area index is within 4.8–6.8 $m^2\ m^{-2}$, with a mean value of 6.2 $m^2\ m^{-2}$. The monthly amount of litterfall is comparable throughout the year, suggesting limited seasonal variations of the leaf area index.

Soils consist mainly of red-yellow podzolic soils (Malaysian classification), also known as Ultisols (soil taxonomy of the United States Department of Agriculture), with high sand content (62–72%), accumulation of nutrients at the surface horizon, low pH (4.0–4.3), and high porosity (54–68%). Ultisols, classified as argillic soil, are representative of the Southeast Asian tropics, contrary to Oxisols, primarily distributed in the African and South American tropics.

Mean annual rainfall was approximately 2,740 mm (5) at Miri Airport (20 km from the Lambir study site) in 1968–2001 and 2,751 mm at the Lambir study site in 2010–2019. The long-term record at Miri Airport exhibited large interannual variations, with a maximum annual rainfall of 3,499 mm in 1988 and a minimum of 2,125 mm in 1976. The seasonal rainfall cycle was similar at Miri Airport and at the Lambir study site: The drier months were February to September, and the wetter months were October to January. The mean annual temperature at the Lambir study site in 2010–2019 was 26.2 °C, with limited seasonal variations.

Measurements of Eddy-Covariance Flux and Environmental Variables. A 4-ha (200 m × 200 m) square experimental plot was established in the Lambir Hills National Park on a north-south gentle slope (inclination of 5° or less) with an approximate length of 2,000 m. The experimental plot was gridded into 400 (20 × 20) subplots of 10 m × 10 m. A 90-m-tall canopy crane with a 75-m-long rotating jib was constructed in 2000 at the center of the plot to access tree crowns. Observational floors of the canopy crane were dedicated to eddy-covariance flux and above-canopy meteorological measurements. A solar radiometer (MS401, EKO Instruments, Japan) for R_s measurements and a tipping-bucket rain gauge (RS102, Ogasawara Keiki, Japan) for P collection were installed on the top floor of the crane, 85.8 m above the forest floor. A temperature and relative humidity sensor (HMP35A, Vaisala, Finland) with a passive ventilation shield was installed at a height of 60.0 m to measure T_a and derive D. A set of identical ventilated sensors (HOBO Pro v2 U23-002 data loggers, Onset, United States of America) was also used for additional T_a and relative humidity measurements at heights of 44.0 m, 32.0 m, 25.0 m, 13.0 m, 5.0 m, and 0.5 m. Volumetric soil moisture content was measured in three subplots using time-domain reflectometry (TDR) sensors (CS616, Campbell Scientific) inserted at depths of 0.1 m, 0.3 m, 0.6 m, and 1.0 m below the forest floor, and Θ was calculated as the weighted mean soil moisture content in the 0.0–0.5 m soil layer using data from the 0.1 m, 0.3 m, and 0.6 m sensors.

Three-dimensional wind speeds (u) and CO_2 and H_2O concentrations were sampled at 10 Hz using a three-dimensional sonic anemometer (CSAT3, Campbell Scientific) for wind speed and an open-path CO_2/H_2O analyzer (LI-7500, Li-Cor) for gas concentrations, both installed at a height of 60.2 m, approximately 20 m above the mean canopy height. The canopy crane fetches along the slope are approximately 1,500 and 500 m in the north and south directions, respectively. The annual-mean dominant wind flows from the north, with minimum fetches required to cover 80% of the source area of approximately 1,000 m in the north direction and 500 m in the south direction (37). The forest canopy is deep, with a source, i.e., a leaf-scale photosynthesis and evapotranspiration position, in its vertical upper part. Resultantly, because the sampling height was approximately 1.5 times the canopy height, the effect of topography on eddy covariance measurements at the studied forest stand could be neglected (38).

Time series were constructed from these measurements. Variances and covariances required for eddy-covariance flux estimates were calculated over a 30-min averaging interval with the EddyPro software (version 7.0.6, Li-Cor). Spikes identified in the vertical wind speed and gas concentration time series were considered out-of-range data points and were replaced with values linearly interpolated from the adjacent data points (39). Coordinate correction with the double-rotation method (40) was applied to orient the mean wind direction along the x-axis and set the mean vertical wind speed to zero. Detrending was performed using block averaging. A frequency-response loss correction was applied to compensate for flux losses at high frequencies (41). A correction for the air density fluctuation effect caused by air temperature and atmospheric H_2O concentration was applied using the Webb–Pearman–Leuning method (42). To eliminate aberrant eddy-covariance flux values, occurring mainly during rainfall events, outlier detection was conducted by identifying instrumental issues, poorly developed turbulent regimes, and nonstationary conditions (43). Additionally, 30-min rolling mean eddy-covariance flux values were calculated over each monthly-mean diurnal cycle; results smaller than 1Q−1.5IQR or larger than 3Q+1.5IQR (where 1Q, 3Q, and IQR represent the first and third quartiles and the interquartile range, respectively) were considered outliers.

Air samples were collected with gas inlets placed at 44.0 m, 32.0 m, 25.0 m, 13.0 m, 5.0 m, and 0.5 m above ground. CO_2 concentrations in the samples were measured with an infrared gas analyzer (LI-820, Li-Cor). In-canopy CO_2 storage flux was determined by quantifying the rate of change of the CO_2 concentration in the canopy air column with the Integrated Carbon Observation System (ICOS) methodology (44). The median of absolute deviation about the median (MAD) was applied to identify and eliminate in-canopy CO_2 storage flux outliers (45).

The NEE was then derived as the sum of the in-canopy CO_2 storage flux and the above-canopy CO_2 eddy-covariance flux. Energy balance correction (*SI Appendix*, Fig. S7), low-turbulence NEE filtering with multiple friction velocity thresholds, and reference NEE determination followed the data processing steps developed for the FLUXNET2015 dataset (46). Additionally, NEE was separated into GPP and R_{eco} for this analysis, using a flux-partitioning algorithm that defines the R_{eco} temperature sensitivity at the half-hour timescale (47). The marginal distribution sampling method [MDS; (47)] was used to fill the temporal gaps in the ET and NEE data and to select observation days for which eddy-covariance flux values, classified (46) as "measured" (quality control flag of 0) or "filling value with high confidence level" (quality control flag of 1), would account for more than 50% of the total daily data. To validate the MDS, artificial gaps were generated within the ET and NEE datasets by randomly removing 25% of the complete half-hourly data. Three different gap lengths were defined (48): 30 d (50% of the generated gaps), 7 d (30% of the total), and 1 d (20% of the total). The artificially gap-filled MDS data were then compared with the observations. We identified significant uncertainties but limited biases in the half-hourly data, with a rmse of 2.46 mmol m^{-2} s^{-1} and 7.90 μmol m^{-2} s^{-1} for ET and NEE, respectively, and linear regression line slopes of 0.843 (Pearson's correlation coefficient, $R^2 = 0.817$) and 0.846 ($R^2 = 0.736$) for ET and NEE, respectively. Thus, we only used data with a quality control flag of 0 to analyze diurnal variations (*SI Appendix*, Fig. S5). For annual-timescale analyses, we relaxed the selection criterion to include data with quality control flags of 0 and 1. The resulting number of days with available eddy-covariance flux data was 578 for both NEE and ET during El Niño events; 737 and 717 d for ET and NEE, respectively, during La Niña events; and 1,468 and 1,435 d for ET and NEE, respectively, under neutral conditions.

Inverse Eddy-Covariance Flux Model. In this study, we used the inverse eddy-covariance flux model of Ueyama et al. (18) and adopted a sun/shade radiative transfer scheme, the "two-big-leaf" model (49), for the ecophysiological traits analysis. The model structure, submodels, and model application to actual eddy-covariance flux data are described in *SI Appendix*.

SHAP Value Determination. We used the SHAP metric (19) to identify the main factors contributing to ET and NEE in the different ENSO phases (El Niño, La Niña, and neutral conditions). The SHAP method, developed for cooperative game theory, assigns a value to all input parameters for a specific model prediction, representing a measure of their contribution to the model output. In this study, ET and NEE were predicted separately in the El Niño, La Niña, and neutral phases with a tree-based machine-learning algorithm, the gradient-boosted regression trees model (20). We set daily values of R_s, G_c, D, T_a, u, V_{cmax25_BL}, P, m_{BB}, and Θ as input parameters. Tenfold cross-validation was applied during the model training process to optimize model parameters. Mean absolute SHAP values for the input parameters (Fig. 3 *A* and *B*) indicated the main controlling factors for ET and NEE in each ENSO phase.

Data, Materials, and Software Availability. MS Excel file has been deposited in AsiaFlux Database (http://asiaflux.net/index.php?page_id=76) (50).

ACKNOWLEDGMENTS. We are grateful to Forest Department Sarawak, Malaysia, for their support during fieldwork. We also thank Tohru Nakashizuka, Masakazu Suzuki, Tetsukazu Yahara, and Lip Khoon Kho for their support, as well as numerous colleagues who helped with the fieldwork. This study was funded by the Core Research for Evolutional Science and Technology funding program of the Japan Science and Technology Agency, the Global Centers of Excellence Program of the Japan Society for the Promotion of Science, and by grants from the Ministry of Education, Culture, Sports, Science and Technology of Japan (Grant Nos. 21H05316 and 21H02229). We thank Eric Dupuy, from Edanz (https://jp.edanz.com/ac), for editing a draft of this manuscript.

Author affiliations: [a]Department of Forest Science, Graduate School of Agricultural and Life Sciences, The University of Tokyo, Yayoi, Tokyo 113-8657, Japan; [b]Department of Subtropical Agro-Environmental Sciences, Faculty of Agriculture, University of the Ryukyus, Nishihara, Okinawa 903-0213, Japan; [c]Shiiba Research Forest, Kyushu University, Shiiba, Miyazaki 883-0402, Japan; [d]Department of Environmental Sciences and Technology, Graduate School of Agriculture, Osaka Metropolitan University, Sakai 599-8531, Japan; [e]Institute for Space-Earth Environmental Research, Nagoya University, Nagoya, Aichi 464-8601, Japan; and [f]Water Resources Research Center, University of Hawai'i at Mānoa, Honolulu, HI 96822

1. C. Beer *et al.*, Terrestrial gross carbon dioxide uptake: Global distribution and covariation with climate. *Science* **329**, 834–838 (2010).
2. Y. Pan *et al.*, A large and persistent carbon sink in the world's forests. *Science* **333**, 988–993 (2011).
3. D. V. Spracklen, S. R. Arnold, C. M. Taylor, Observations of increased tropical rainfall preceded by air passage over forests. *Nature* **489**, 282–285 (2012).
4. R. Portmann *et al.*, Global forestation and deforestation affect remote climate via adjusted atmosphere and ocean circulation. *Nat. Commun.* **13**, 1–11 (2022).
5. T. Kumagai *et al.*, Annual water balance and seasonality of evapotranspiration in a Bornean tropical rainforest. *Agric. For. Meteorol.* **128**, 81–92 (2005).
6. W. Cai *et al.*, Increasing frequency of extreme El Niño events due to greenhouse warming. *Nat. Clim. Change* **4**, 111–116 (2014).
7. W. Cai *et al.*, Increased frequency of extreme La Niña events under greenhouse warming. *Nat. Clim. Change* **5**, 132–137 (2015).
8. A. Capotondi, Extreme La Niña events to increase. *Nat. Clim. Change* **5**, 100–101 (2015).
9. C. Huntingford *et al.*, Simulated resilience of tropical rainforests to CO_2-induced climate change. *Nat. Geosci.* **6**, 268–273 (2013).
10. D. Lawrence, K. Vandecar, Effects of tropical deforestation on climate and agriculture. *Nat. Clim. Change* **5**, 27–36 (2015).
11. J. Liu *et al.*, Contrasting carbon cycle responses of the tropical continents to the 2015–2016 El Niño. *Science* **358**, eaam5690 (2017).
12. H. Hashimoto *et al.*, El Niño-Southern Oscillation–induced variability in terrestrial carbon cycling. *J. Geophys. Res.: Atmos.* **109**, D23110 (2004).
13. G. Koren *et al.*, Widespread reduction in sun-induced fluorescence from the Amazon during the 2015/2016 El Niño. *Philos. Trans. R. Soc. B: Biol. Sci.* **373**, 20170408 (2018).
14. M. Kondo *et al.*, Land use change and El Niño-Southern Oscillation drive decadal carbon balance shifts in Southeast Asia. *Nat. Commun.* **9**, 1–11 (2018).
15. N. C. Parazoo *et al.*, Influence of ENSO and the NAO on terrestrial carbon uptake in the Texas-northern Mexico region. *Global Biogeochem. Cycles* **29**, 1247–1265 (2015).
16. M. Bretfeld, B. E. Ewers, J. S. Hall, Plant water use responses along secondary forest succession during the 2015–2016 El Niño drought in Panama. *New Phytol.* **219**, 885–899 (2018).
17. V. A. H. F. dos Santos *et al.*, Causes of reduced leaf-level photosynthesis during strong El Niño drought in a Central Amazon forest. *Global Change Biol.* **24**, 4266–4279 (2018).
18. M. Ueyama *et al.*, Inferring CO_2 fertilization effect based on global monitoring land-atmosphere exchange with a theoretical model. *Environ. Res. Lett.* **15**, 084009 (2020).
19. S. M. Lundberg, S.-I. Lee, A unified approach to interpreting model predictions. *Adv. Neural Inf. Process. Syst.* **30** (2017).
20. T. Chen, C. Guestrin, "Xgboost: A scalable tree boosting system" in *Proceedings of the 22nd ACM SIGKDD International Conference on Knowledge Discovery and Data Mining* (2016), pp. 785–794.
21. R. Leuning, A critical appraisal of a combined stomatal-photosynthesis model for C_3 plants. *Plant, Cell Environ.* **18**, 339–355 (1995).
22. N. Restrepo-Coupe *et al.*, What drives the seasonality of photosynthesis across the Amazon basin? A cross-site analysis of eddy flux tower measurements from the Brasil flux network. *Agric. For. Meteorol.* **182**, 128–144 (2013).
23. L. R. Hutyra *et al.*, Seasonal controls on the exchange of carbon and water in an Amazonian rain forest. *J. Geophys. Res.: Biogeosci.* **112**, G03008 (2007).
24. G. J. Collatz, J. T. Ball, C. Grivet, J. A. Berry, Physiological and environmental regulation of stomatal conductance, photosynthesis and transpiration: A model that includes a laminar boundary layer. *Agric. For. Meteorol.* **54**, 107–136 (1991).
25. B. E. Medlyn *et al.*, Reconciling the optimal and empirical approaches to modelling stomatal conductance. *Global Change Biol.* **17**, 2134–2144 (2011).
26. G. D. Farquhar, S. von Caemmerer, J. A. Berry, A biochemical model of photosynthetic CO_2 assimilation in leaves of C_3 species. *Planta* **149**, 78–90 (1980).
27. P. G. Jarvis, K. G. McNaughton, "Stomatal control of transpiration: Scaling up from leaf to region" in *Advances in Ecological Research*, A. MacFadyen, E. D. Ford, Eds. (Elsevier, 1986), pp. 1–49.
28. J. Lloyd, G. D. Farquhar, Effects of rising temperatures and [CO_2] on the physiology of tropical forest trees. *Philos. Trans. R. Soc. B: Biol. Sci.* **363**, 1811–1817 (2008).
29. M. Ohashi *et al.*, The effects of an induced short-term drought period on the spatial variations in soil respiration measured around emergent trees in a typical Bornean tropical forest, Malaysia. *Plant Soil* **387**, 337–349 (2015).
30. I. J. Wright *et al.*, Irradiance, temperature and rainfall influence leaf dark respiration in woody plants: Evidence from comparisons across 20 sites. *New Phytol.* **169**, 309–319 (2006).
31. P. Meir, D. B. Metcalfe, A. C. L. Costa, R. A. Fisher, The fate of assimilated carbon during drought: Impacts on respiration in Amazon rainforests. *Philos. Trans. R. Soc. B: Biol. Sci.* **363**, 1849–1855 (2008).
32. S. D. Wullschleger, Biochemical limitations to carbon assimilation in C_3 plants–A retrospective analysis of the A/C_i curves from 109 species. *J. Exp. Bot.* **44**, 907–920 (1993).
33. T. Kenzo, T. Ichie, Y. Watanabe, T. Hiromi, Ecological distribution of homobaric and heterobaric leaves in tree species of Malaysian lowland tropical rainforest. *Am. J. Bot.* **94**, 764–775 (2007).
34. O. L. Phillips *et al.*, Drought sensitivity of the Amazon rainforest. *Science* **323**, 1344–1347 (2009).
35. L. Rowland *et al.*, Death from drought in tropical forests is triggered by hydraulics not carbon starvation. *Nature* **528**, 119–122 (2015).
36. T. Kumagai, A. Porporato, Drought-induced mortality of a Bornean tropical rain forest amplified by climate change. *J. Geophys. Res.: Biogeosci.* **117**, G02032 (2012).
37. N. Kljun, P. Calanca, M. W. Rotach, H. P. Schmid, A simple two-dimensional parameterisation for Flux Footprint Prediction (FFP). *Geosci. Model Dev.* **8**, 3695–3713 (2015).
38. B. Chen, M. Chamecki, G. G. Katul, Effects of gentle topography on forest-atmosphere gas exchanges and implications for eddy-covariance measurements. *J. Geophys. Res.: Atmos.* **125**, e2020JD032581 (2020).
39. D. Vickers, L. Mahrt, Quality control and flux sampling problems for tower and aircraft data. *J. Atmos. Oceanic Technol.* **14**, 512–526 (1997).

40. C. B. Tanner, G. W. Thurtell, *Anemoclinometer Measurements of Reynolds Stress and Heat Transport in the Atmospheric Surface Layer* (Department of Soil Science, Wisconsin University–Madison, 1969).
41. J. B. Moncrieff *et al.*, A system to measure surface fluxes of momentum, sensible heat, water vapour and carbon dioxide. *J. Hydrol.* **188**, 589–611 (1997).
42. E. K. Webb, G. I. Pearman, R. Leuning, Correction of flux measurements for density effects due to heat and water vapour transfer. *Q. J. R. Meteorol. Soc.* **106**, 85–100 (1980).
43. D. Vitale *et al.*, A robust data cleaning procedure for eddy covariance flux measurements. *Biogeosciences* **17**, 1367–1391 (2020).
44. L. Montagnani *et al.*, Estimating the storage term in eddy covariance measurements: The ICOS methodology. *Int. Agrophys.* **32**, 551–567 (2018).
45. D. Papale *et al.*, Towards a standardized processing of Net Ecosystem Exchange measured with eddy covariance technique: Algorithms and uncertainty estimation. *Biogeosciences* **3**, 571–583 (2006).
46. G. Pastorello *et al.*, The FLUXNET2015 dataset and the ONEFlux processing pipeline for eddy covariance data. *Sci. Data* **7**, 1–27 (2020).
47. M. Reichstein *et al.*, On the separation of net ecosystem exchange into assimilation and ecosystem respiration: Review and improved algorithm. *Global Change Biol.* **11**, 1424–1439 (2005).
48. S. Zhu, R. Clement, J. McCalmont, C. A. Davies, T. Hill, Stable gap-filling for longer eddy covariance data gaps: A globally validated machine-learning approach for carbon dioxide, water, and energy fluxes. *Agric. For. Meteorol.* **314**, 108777 (2022).
49. D. G. G. de Pury, G. D. Farquhar, Simple scaling of photosynthesis from leaves to canopies without the errors of big-leaf models. *Plant, Cell Environ.* **20**, 537–557 (1997).
50. T. Kumagai, Y. Hata, LHP:Lambir Hills National Park. AsiaFlux Database. https://db.cger.nies.go.jp/asiafluxdb/?page_id=16. Deposited 13 April 2023.